SI-2023-ECCOMAS

Journal of Intelligent Material Systems and Structures

Journal of Intelligent Material Systems and Structures
1–16

DOI: 10.1177/1045389X251341612
journals.sagepub.com/home/jim

Design of a shape-adaptive rotor for the reduction of BLI induced losses in the distorted flow regimes of a scaled turbofan fan rotor

Marcel Seidler[1], Felix Kleinwechter[2], Jonas Voigt[1], Hans Peter Monner[2], Jens Friedrichs[1], Zhuzhell Montano Rejas[2] and Johannes Riemenschneider[2]

Abstract

Within the Cluster of Excellence for Sustainable and Energy-Efficient Aviation SE^{2}A, a blended wing body aircraft is investigated to improve efficiency and carbon emissions of future air transport. By embedding the aircraft engines on the top rear fuselage, parts of the aircraft's wing boundary layer are ingested, which has the potential to further improve the engine's propulsion efficiency. Through the ingestion of low momentum fluid, inflow distortion is induced and the fan rotor operates under increased flow incidence, when passing through the distorted flow regimes. To reduce the thereby arising efficiency and pressure ratio penalties in the aircraft engine, alternative design strategies for the fan stage are required. Within this investigation, an active shape morphing mechanism is introduced, which allows to temporarily adjust the fan blading when the fan rotor is exposed to distorted inflow conditions. By integrating piezoceramic actuators into the rotor blading, the blade staggering and turning can be adjusted with the goal to reduce flow incidence and deviation in the distorted flow regimes. For this investigation, the NASA rotor 67 is chosen as an initial test case and its performance under boundary layer ingestion (BLI) conditions is evaluated. For the shape morphing assessment, FEA morphing simulations are coupled with stationary CFD simulations of the actuated fan rotor geometries under distorted inflow. As the achievable deformations for the NASA rotor 67 are however too small to compensate for the strong distortion effects, a fan re-design is conducted. The re-design follows current ultra-high-bypass-ratio (UHBR) fan concepts with a particular focus on the shape-morphing capability of the rotor. Within this investigation the focus especially lies on three-dimensional design adaptions, such as a hub chord reduction as well as dihedral and sweep. By considering carbon fiber reinforced polymers (CFRP) as blade material, the impact of tailored blade architectures on the morphing behavior is additionally considered.

Keywords

Fan design, shape adaption, boundary layer ingestion

1. Introduction

To increase the energy efficiency of future air transport, new aircraft architectures are investigated. Here, boundary layer ingestion (BLI) is a promising concept to improve overall efficiency. The ingestion of the aircraft structure's boundary layer allows to improve the propulsive efficiency by exploiting the reduced inflow momentum at the engine intake, (Smith, 2023). Within the Cluster of Excellence for *Sustainable and Energy-Efficient Aviation SE^2 A*, a blended wing body aircraft featuring engines embedded on the top rear fuselage is currently researched (Figure 1). The ingestion of low momentum fluid leads to distortion effects in the lower shroud area of the intake. When passing through areas of different flow conditions, the fan experiences flow incidence and instationary aerodynamic effects, which indicates a major drawback of BLI concepts. The dominant inflow condition in the distorted area differ

[1]Institute of Jet Propulsion and Turbomachinery, TU Braunschweig, Braunschweigç Niedersachsen, Germany
[2]Institute of Lightweight Systems, German Aerospace Center (DLR), Braunschweig, Lower Saxony, Germany

Corresponding author:
Marcel Seidler, IFAS, TU Braunschweig, Hermann-Blenk-Straße 37, Braunschweig, Niedersachsen 38108, Germany.
Email: marcel.seidler@tu-braunschweig.de

Data Availability Statement included at the end of the article.

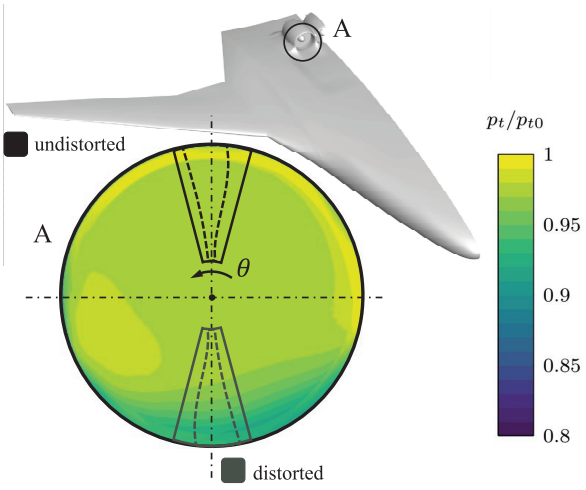

Figure 1. BWB half model with total pressure distortion pattern upstream of the fan due to boundary layer ingestion.

from those of the rotor design point. Especially for modern transonic compressor rotors with an increased tip loading inflow incidence may diminish the BLI benefits through increased losses in the fan stage (Giesecke and Friedrichs, 2019). To align both BLI effects on the overall propulsion efficiency, this research investigates the concept of a shape-adaptive rotor. Adding piezoelectic Macro Fiber Composite™Actuators (MFC) to the blade architecture allows to morph the blade's shape depending on the circumferential position of the rotor (Figure 1). While passing the distorted flow regime, the piezoelectric actuators provoke a specific adaption of the span-wise blade twist and cambering, according to the prevalent flow angle variations induced by the low momentum fluid. With the highest achievable deformations located toward the rotor tip (Seidler et al., 2022), the shape-adaption concept increases the design flexibility where the highest aerodynamic effects of inflow distortion are expected. Based on generic distortion patterns, this research aims to mitigate the drawbacks of inlet distortion through deriving a suitable actuation concept for the distorted flow regimes. First, the transonic NASA rotor 67 (Hathaway, 1986) is transformed into a shape-adaptive system, as previously described by Seidler et al. (2022). As the applied MFC actuators allow for actuation frequencies up to 10 kHz (Smart Material GmbH, 2023), an actuation once per rotation is technically feasible for high-speed fan rotors, such as the chosen test case. For design speed, the blades of the NASA rotor 67 would pass the distorted flow regimes with 267 Hz (Hathaway, 1986), determining the required actuation frequency. Modern UHBR turbofans, which would be employed in BLI engines, require even lower actuation frequencies in the range of $50\,s^{-1}$ (Giesecke and Friedrichs, 2019). By investigating the effects of BLI on the stage performance, actuation strategies are specified and a structural morphing assessment for different actuation concepts is carried out. To evaluate the potential of the feasible shape variations, representative stationary CFD simulations are conducted for a rotor and stator passage with maximum distortion.

The initial findings are consequently transferred to the geometry of a scaled turbofan rotor with main dimensions comparable to current UHBR fan designs (Seidler et al., 2024a). The rotor reference design is consequently varied to increase its morphing potential and thus the achievable impact on the fan stage performance under distorted inflow conditions. This design study focuses on three-dimensional design adaptions, such as a hub chord length reduction and the application of sweep and dihedral. Alternative blade materials are also considered. While the initial morphing investigations are conducted with titanium alloy blades, the application of carbon fiber reinforced polymers (CFRP) allows for a tailored blade architecture. By optimizing the orthotropic material properties induced by the orientation of the carbon fiber material, the tailored CFRP blade supports the deformability toward a piezoelectric actuation while withstanding the high centrifugal loads during operation. With that, this study aims to investigate piezoactive rotor blading as an alternative to pitch-variable fan blading (Mennicken et al., 2022), variable nozzle geometries (Hall and Crichton, 2006) or an adaption of the stator geometry (Giesecke, 2022) to mitigate BLI induced off-design drawbacks. In comparison, piezoelectric actuation concepts inherit a lower mechanical complexity and weight, while offering the means to individually control the voltage supply for single blades and fractions of the full rotor annulus. Despite remarkable achievements for the active morphing of aircraft wings (Barbarino et al., 2014), wind turbine blades (Krawczyk et al., 2013) as well as simplified stator cascades (Abate and Riemenschneider, 2025), an application of piezoelectric actuators to the complex three-dimensionally shaped blades of a turbofan rotor has so far not been conducted. Suman et al. (2017) experimentally applied Shape Memory Alloy (SMA) actuators to the polymeric blades of an automotive cooler fan, thereby increasing its cambering and therefore the loading coefficient, especially during part-load operation. In a numerical approach, Tweedt (2013) investigated the impact of twist adaptive UHBR turbofan blades on the operating range and efficiency of two fan rotor geometries. Although the deformations were assumed to be variable in span-wise direction, no actuation concept was specified. A positive effect on the surge margin during take-off conditions was however observed, indicating the potential of piezoelectric fan blading for an overall higher propulsive efficiency throughout the flight mission. The positive effect of a piezoactive fan

on the overall fuel consumption during different flight missions was later confirmed by Seidler et al. (2024b) through mission-based thermodynamic cycle calculations. The specific effect of piezoelectrically deformed blade profiles on the blade-shock interaction of pre-compression blade profiles is reported in Li et al. (2023). Here, the choking behavior of a simplified 2D cascade was altered by piezoelectrically controlling the pre-compression strength of the profile section investigated. Within the research presented, a numerical model of an established actuation concept (Krone et al., 2017) is therefore combined with state-of-the art fan rotor geometries. Thereby the comprehensive efforts of the authors to evaluate aerodynamic losses due to boundary layer ingestion (Voigt and Friedrichs, 2021) and the transformation of conventional fan geometries into shape-adaptive systems for an increased off-design efficiency (Seidler et al., 2022) are consolidated.

2. Methodology

2.1. Derivation of the distortion pattern

To generate an authentic BLI distortion pattern, compressible, steady state 3D-RANS simulations of the SE^{2}A blended wing body (BWB, Figure 1) reference design were conducted. The aircraft geometry and flight conditions are based on design studies carried out for the next design iteration of the BWB, as described in Karpuk et al. (2020). Nacelles designed following the methodology described in Benjamin et al. (2020) were integrated onto the top rear of the aircraft fuselage. The DLR TAU-Code (Schwamborn et al., 2006), a finite-volume-based Navier-Stokes solver, is used for the CFD simulation, while the mesh is generated with CENTAUR. The mesh is unstructured except for prism layers in the near-wall regions. For turbulence modeling, the k- ω model is applied. The BWB is modeled as a half model, as shown in Figure 1. The plane spanned by the vertical axis and the axis pointing in flight direction is therefore defined as symmetry plane. All walls are considered viscous and adiabatic. The amount of mass flow leaving the domain at the engine's intake and re-entering the domain at the engine exhaust is determined by the chosen operating point. For both interfaces a mass flow boundary condition is applied. Far-field conditions at the domain boundary are set to ISA (ISO 2533:1975, 1975) conditions corresponding to the cruise operating point of the aircraft. After the CFD simulation of the aircraft is converged, the total pressure field at the nacelle inlet is extracted and normalized using the far field total pressure p_{t0}. By generalizing the total pressure distortion with respect to the relative channel height, a transfer of the distortion pattern's shape to a different test case, with varying design conditions and main dimensions becomes feasible.

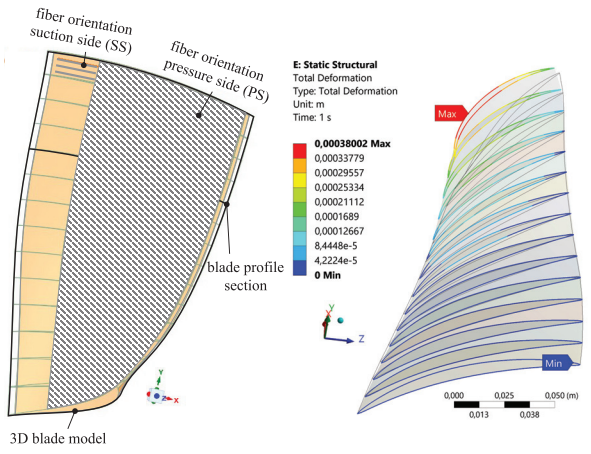

Figure 2. Actuator models based on blade reference sections (left) and simulated deformations at the blade sections (right).

2.2. Stage performance evaluation

To evaluate the aerodynamic performance of the fan stage, 3D steady-state passage simulations are conducted in Ansys CFX. For the rotor and stator domain with one blade each, a structured mesh is created with $y^+ = 1$ at all domain walls for the aerodynamic design point.

The dimensionless wall distance y^+ is defined as

$$y^+ = \frac{u_* y}{\nu} \quad \text{with} \quad u_* = \sqrt{\frac{\tau_W}{\rho}}, \tag{1}$$

with the friction velocity u_* at the nearest wall, the distance to the wall y, the local kinematic viscosity ν, the wall shear stress τ_W, and the density ρ. Selecting $y^+ = 1$ for the first mesh cell near a viscous wall allows to sufficiently resolve the viscous sublayer, avoiding additional models for the fluid's boundary layer. A k-ω turbulence model is used and the speed lines are created by gradually increasing the static pressure at the domain outlet until residual and mass flow divergence indicates the numerical stability limit. For the consideration of BLI effects, the radial total pressure distortion p_t/p_{t0} is applied as a domain inlet condition of the rotor passage.

2.3. Structural morphing methodology

Mitigating the BLI induced drawbacks requires a specific variation of the span-wise blade angles. After these requirements are derived from the CFD results, an angular optimization target for the structural design methodology is defined. For the structural morphing simulation, the blade and actuator geometries need to be created. Here, the blade sections of the reference blade geometry are used to derive a 3D CAD model of the rotor (see Figure 2). These sections also serve as a

reference for the definition of the actuators, which are applied onto the suction (SS) and pressure side (PS) of the blade (see Figure 2). The actuators extend over the entire blade span, while in chord-wise direction the actuator dimensions are defined as a fraction of the blade chord l. The maximum chord-wise extent of the actuators is determined by the minimum blade thickness that would be required for an integration of the actuators into the blade architecture. As the profile sections become thinnest at the blade tip, it is the tip section design that determines the feasible actuator length in chord-wise direction.

After creating 3D models of the blade and actuator geometries, material properties are assigned. In the structural model, the piezoelectric actuators are implemented as MFC actuators, which consist of expanding/contracting piezoceramic fibers (Smart Material GmbH, 2023). Depending on the aerodynamic morphing target suitable piezoceramic fiber orientations are specified for the MFC actuators, which together with the actuator dimensions and the actuation mechanism determines the deformation behavior of the blade. The blade body can either be designed as a full titanium rotor or as a composite structure. Both materials are investigated in this research. For the composite structure, carbon fiber reinforced polymers are applied. Within this investigation, layers of *Epoxy Carbon UD (230 GPa) prepreg* and *Epoxy Carbon Woven (230 GPa) prepreg* are used in combination with *Resin Epoxy* as the drop-off and cut-off material (Ansys Inc, 2022b). The CFRP blade additionally exhibits an optional foam core (*San Foam*, 103 kg m^{-3}). For the modeling of the blade's laminate structure in Ansys Composite PrepPost (ACP), surface models are required as an input. Therefore, surface meshes of the blade's suction and pressure side are created instead of a fully meshed 3D volume model. Starting from the meshed surfaces, the layers of the laminate are defined, which results in two blade halves. To prevent an overlapping between the blade halves, the layers are cut at a mid-surface, which is defined by the blade sections' camber lines (see Figure 3). The resulting model is composed of shell elements that are transformed into solid elements for the finite element analysis (FEA). In Ansys ACP, this conversion is executed by extruding from the meshed surfaces of the suction and pressure sides. Accompanied by guided extrusions in the root and tip areas and an adaptation to the mid-surface, the outcome is a solid model that is devoid of overlaps, gaps or offsets. The blade halves are joined utilizing a contact bonding approach. In case an isotropic material like titanium is used, an unstructured 3D mesh is used for the 3D blade geometry. After the structural models are created for the actuators and the blade body (composite or isotropic), the actuators are placed onto the blade surface. To transfer the deformations from the actuators into the blade's structure, a contact bonding approach between actuators and blade is applied, which also results in combined load bearing between the components. The definition of boundary conditions provides the final step for the structural model (Figure 3), from which then the morphing can be calculated.

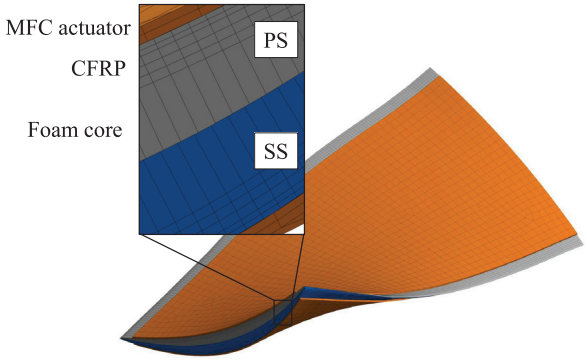

Figure 3. Layers and composition of the structural CFRP model with MFC actuators.

During the preliminary experimental investigations, conducted by Krone et al. (2017) an electric field was exploited to evoke the shape variation of the MFC actuators. In the structural methodology presented, the actuator's behavior is approximated with a thermal expansion analogy, as described by Kovalovs et al. (2007) and later applied in Kleinwechter et al. (2024). The analogy approximates the deformation that would normally be reached through the introduction of the electric field by defining suitable thermal boundary conditions. To consider the risk of actuator damage due to the centrifugal pre-loading and a maximization of the actuation voltage the applied voltage is limited to $V_a = 1000\,V$ for expansion and $V_a = -333\,V$ for contraction. After the structural morphing simulation, the span-wise deformations are evaluated for the aerodynamic reference sections. Preserving the profile sections throughout the FEA simulation simplifies the re-engineering of the deformed rotor geometry and the morphing evaluation according to the aerodynamic blade angle definitions (Figure 4).

The structural morphing results are therefore exported for the aerodynamic design sections. As displayed in Figure 4, an extensive post processing routine transforms the directional displacement for every mesh node into a span-wise aerodynamic blade angle morphing, such as the variation of the leading edge metal angle

$$\Delta\kappa_1(r) = \kappa_{1,\mathrm{def}}(r) - \kappa_{1,\mathrm{ref}}(r), \tag{2}$$

with

$$\kappa_1(r) = \lambda(r) + \alpha_1(r), \tag{3}$$

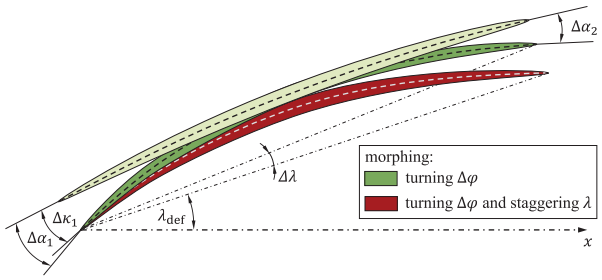

Figure 4. Schematic blade section morphing with angular variations.

where *def* refers to the morphed shape and *ref* to the blade angles of the reference geometry. The variation of the blade turning is calculated as follows:

$$\Delta^2\varphi(r) = \Delta\varphi_{\text{def}}(r) - \Delta\varphi_{\text{ref}}(r) \tag{4}$$

With that, a positive angular morphing value corresponds to an increase compared to its original value.

2.4. Blade design

For the turbofan design and its variants, streamline curvature (SLC) design calculations are conducted, following the methodology described in Seidler et al. (2024a). By choosing a span-wise load distribution for the rotor, the SLC procedure allows to estimate the meridional distribution of relevant flow quantities, defining the inflow as well as outflow angles of the rotor. Based on those, a suitable rotor geometry is derived and transferred to the structural morphing analysis. An efficiency evaluation based on Bullock and Johnson (1965) and Cunnan et al. (1978) allows to assess the enthalpy rise through the rotor and to iterate the required design pressure ratio for a pre-selected mass flow. The profile sections are defined with an equal spacing in span-wise direction. The main dimensions that determine the meridional shape of the blade, are the hub-to-tip ratio ν_{ht} that defines the blade length in radial direction and the aspect ratio AR that—with the hub to tip ratio fixed—yields the chord length l of the rotor. By selecting a maximum camber position and deriving the relative flow angles, where the meridional sections intersect with the leading and trailing edge of the rotor blade, the camber of the respective blade profile is modeled. Within this research a parabolic mean camber is combined with a thickness distribution defined through the Class Shape Function methodology (Giesecke et al., 2018). For the rotor design wedge shaped profiles, commonly used for transonic inflow conditions, are chosen, by relying on a thickness modeling extension, introduced by Seidler and Friedrichs (2022). This methodology allows to specifically adapt the leading edge thickness as well as the suction side curvature to control pre-shock flow acceleration and with that shock losses.

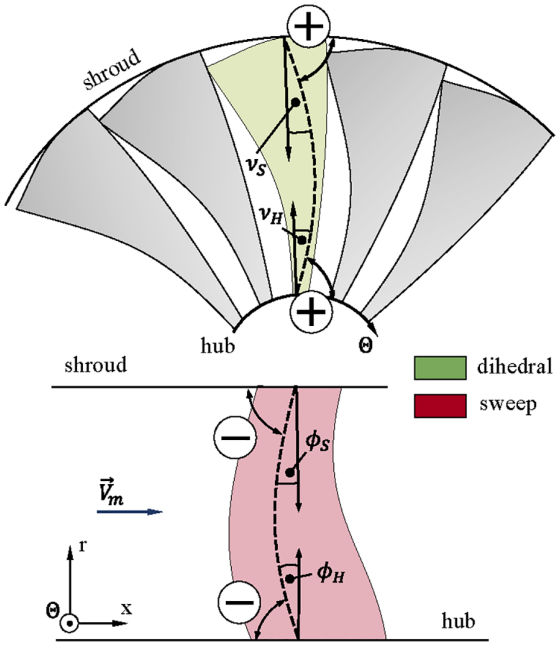

Figure 5. Schematic visualization of the sweep and dihedral angles, defined for the stacking line of the rotor (dashed).

For the implementation of sweep and dihedral, the sweep (ϕ_H, ϕ_S) and dihedral (ν_H, ν_S) angles are defined at the hub and shroud following Eggers et al. (2020). The respective angles are used to create a circular arc between hub and shroud that defines the span-wise stacking line. Separate arc contours are used for sweep and dihedral, as displayed in Figure 5. Depending on the radial blade position, the stacking line determines the respective profile displacement in their staggered chord direction (sweep) or perpendicular (dihedral) to it. The sign of the angles defines the type of sweep and dihedral. As displayed in Figure 5, a positive dihedral angle implies an obtuse angle between blade suctions side and end-wall contour. A negative leading edge sweep angle indicates a sharp angle between channel end-walls and the blade leading edge. The blade schematically depicted in Figure 5, protrudes toward the incoming flow V_m at the hub, while leaning backwards at the shroud, both implying negative end-wall sweep angles. In addition to the displacement of the profile sections, aircraft wing design has shown that the application of sweep leads to a load variation due to a local lift reduction of the corresponding profile section. To alter the load variation, the chord length l is estimated as the fraction of the original chord length l_o and the cosine of the local sweep angle ϕ, as described by Schlichting and Truckenbrodt (2001):

$$l = \frac{l_o}{cos(\phi)} \tag{5}$$

This correlation is well known from aircraft wing design and has been applied in previous research (Eggers et al., 2020; Giesecke and Friedrichs, 2019). Thereby the sweep effect on the span-wise load distribution is mitigated and the aerodynamic designs remain comparable within this investigation.

3. Results

3.1. Impact of BLI on stage performance

Three speed lines at 100%, 85%, and 70% design speed are evaluated for undistorted flow conditions (black) and a distorted blade passage (gray; Figure 1). In Figure 6 the isentropic efficiency η_{is} and the pressure ratio Π are displayed, depending on the absolute mass flow $\dot{m}_{abs}$ through the stage.

Through the total pressure deficit upstream of the rotor, the required rotor work input increases. The blade loading is elevated, especially affecting the tip region, where the distortion effects are most prominent. Ingesting the boundary layer of the blended wing body's fuselage reduces the meridional velocity toward the fan. Thereby, the mass flow over all speed lines is decreased. Combined with a constant rotational speed, the relative inflow angle is raised, causing flow incidence, which becomes especially critical under part-load operating conditions. Under distorted inflow conditions, the characteristic increase in tip loading during part-load becomes more critical, which results in the surge margin reduction for all speed lines displayed in Figure 6. The deficit in design point mass flow is highest for the 100% speed line, as the rotor performance is highly sensitive toward the unique incidence condition. Although the inlet distortion reduces the relative inflow Mach number, the flow remains transonic in the outer span of the rotor. With a passage shock occurring in the upper flow regimes of the rotor, BLI mainly affects the unique incidence condition and its characteristic mass flow. With that, flow separation within the blade passage is mainly driven by the strength and position of the passage shock. A similar effect is visible for the right branch of the 85% speed line, where the dependency on the unique incidence condition accelerates the mass flow deficit. With a further reduction of the mass flow a reduced percentage of the rotor operates under the unique incidence condition. With that the rotor performance is increasingly affected through a steeper inflow and the earlier onset of flow separation in the blade passage. The combination of raised blade loading and earlier flow separation are also the dominant effects for the 70% speed line, where the reduction in surge margin is strongest. A significant passage shock only occurs in the upper 15% of the rotor, when the stage operates close to its choke limit. This leads to the higher mass flow deficit toward increased operating mass flow rates. For all speed lines the achievable peak efficiency is reduced, when operating under distorted inflow conditions. With 1.15% the efficiency deficit is highest for the 70% speed line, driven by the increased flow incidence. For higher relative inflow Mach numbers, the BLI effect is dampened by the occurrence of a passage shock resulting in a lower peak efficiency deficit of 0.65% for the 100% speed line (Figure 6).

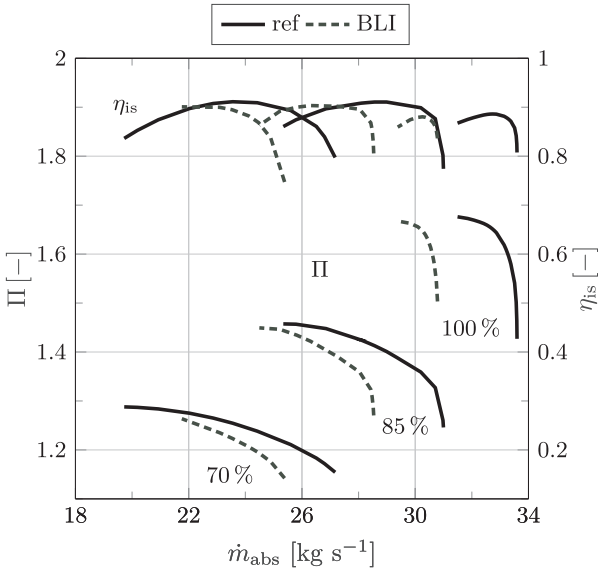

Figure 6. Performance of the reference NASA rotor 67 with upstream distortion (gray) and undistorted inflow (black).

Conclusions: The main influence of BLI is the increase of flow incidence at the blade tip. This causes a mass flow displacement for operating points, where choking occurs within the rotor. For part-load operation, efficiencies are additionally diminished and a reduction of the surge margin becomes apparent. An offset between peak efficiencies and the current operating point is created, which depending on the working line further decreases operational efficiencies in case the fan rotor experiences distorted inflow conditions.

3.2. Rotor morphing results

The drawbacks of BLI on the fan stage performance are driven by the flow incidence caused by the low momentum flow in the distorted regimes of the fan face. Neglecting the impact of the blade thickness and camber on the flow angles, flow incidence is caused or compensated by a variation of the leading edge metal angle:

$$\Delta i = \Delta\kappa_1 = \Delta\lambda + \Delta\alpha_1 \tag{6}$$

To reduce flow incidence, two actuator configurations are derived that temporarily allow to increase the leading edge metal angle κ_1, when the blade passes through

Table 1. Details of the actuator configurations applied.

Configuration	o_{PS}	Mode (PS)	o_{SS}	Mode (SS)
Turning +	6°	Contraction	2°	Expansion
Stagger +	50°	Expansion	51°	Expansion

the distorted flow regimes. A morphing of the leading edge metal angle κ_1 is either feasible through a stronger blade staggering λ or through a higher blade leading edge camber angle α_1 (Figure 4). For both approaches, a suitable actuator configuration is assessed. The actuator configurations considered are summarized in Table 1.

Figure 7 summarizes the achievable variation of the metal angle $\Delta\kappa_1$, of the profile turning $\Delta^2\varphi$ and the morphing impact on the blade staggering $\Delta\lambda$ for both actuator configurations, depending on the radial position along the rotor leading edge r_1.

Through the centered location of maximum thickness and camber position, an increase of the leading edge camber angle requires actuators that maximize the blade turning. With the orientation of the piezoelectric fibers in the MFC actuator determining the actuation direction and the cantilever of the forces applied into the blading, the structural design yields a piezoelectric fiber orientation that approximates the streamline slope of the tip section. This results in a MFC actuator fiber orientation of 2° for the suction side (o_{SS}) and 6° for the pressure side (o_{PS}, see Table 1). Through a dominant expansion of the suction side actuator and a supporting contraction of the pressure side actuator, an increase of the blade turning by a maximum of 0.89° at the blade tip is achieved (*turning +*). The deflection of the stagger angle $\Delta\lambda$ with a maximum of 0.06° is negligible compared to the dominant turning variation. This results in a maximum incidence correction of $\Delta\kappa 1 = 0.61°$ at 100% blade height. With increasing fiber angles, the morphing impact on the blade turning becomes weaker and the blade staggering is increasingly affected. Depending on the blade's main dimensions, the structural design for an improved stagger angle morphing yields a fiber orientation of 51° for the suction side and 50° for the pressure side. An expansion of both actuators results in an increase of the stagger angle by 0.36° at the blade tip (*stagger +*). The adaption of the blade turning remains above −0.2° with a local turning reduction maximum at 72% blade height. This determines a maximum leading edge metal angle adaption of 0.42°. For the stagger adaption scenario *stagger +*, the achievable leading edge metal angle variation is concentrated in the upper 30% of the blade. In comparison, the κ_1 morphing for the *turning +* scenario extends further toward the blade's root with perceptible deformations already occurring above 50% blade height.

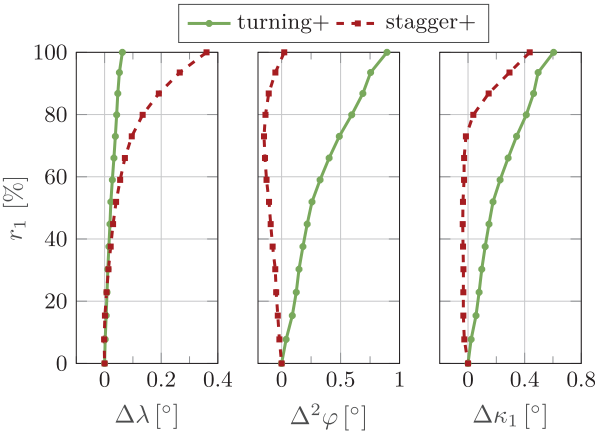

Figure 7. Achievable shape adaption for a stagger and a leading edge camber angle morphing.

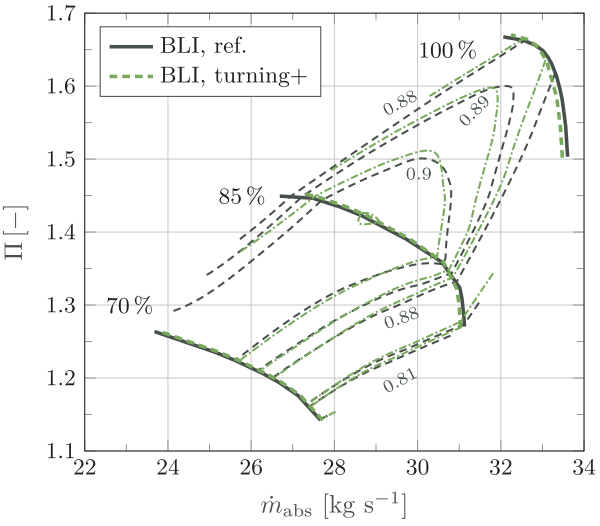

Figure 8. Effect of a blade turning morphing on the rotor performance under BLI influence, displayed for different rotational speeds and the efficiency iso lines.

3.3. Morphing effect on stage performance

A higher profile turning of the rotor (*turning +*) locally increases blade loading (Figure 8). During part-load operation, the characteristic load redistribution toward the blade tipis amplified, which elevates the overall pressure ratio Π, but also provokes a reduction of the surge margin as flow diffusion is accelerated. Through the increment in leading edge metal angle, flow incidence is reduced for those fractions of the rotor, which operate with the leading edge bow shock detached. As the radial fraction of the rotor which operates outside of unique incidence increases toward the surge limit, a slight improvement of the stage efficiencies with reduced mass flow rates is visible for the 100% speed line. For lower design speeds, the increased pressure

ratios and isentropic efficiencies η_{is} become the dominant effect of the shape morphing, as the dependency on the unique incidence condition is less prominent. For the 70% speed line, the relative inflow Mach numbers become too small for the unique incidence condition to have a significant influence on the overall performance variation, which results in a slightly elevated speed line compared to the distorted reference shape. For 100% and 85% design speed, the speed line variation toward the choke mass flow is dominated by the shock occurring in the blade passage. According to the unique incidence condition, an increase in leading edge metal angle reduces the mass flow through the passage, leading to the sinistral shift of the speed line visible in Figure 8. Additionally, the higher leading edge metal angle and overall blade turning correlates with an increase in suction side curvature. The occurring shock pattern is highly sensitive to increments in suction side curvature, as the pre-shock flow is accelerated. This results in an elevated shock strength and higher shock losses. The resulting reduction of the stage efficiencies is especially dominant for the 100% speed line.

An increase of the stagger angle (*stagger* +) constantly shifts the speed lines toward lower mass flow rates (Figure 9). The higher leading edge metal angle κ_1 either alters the unique incidence mass flow for high flow rates and rotational velocities or allows for an incidence correction, in case the majority of the blade span operates under subsonic inflow or with a detached leading edge bow shock. Through a slight reduction of the overall blade turning between 40% and 90% blade height (Figure 7), the achievable pressure ratios are lower for all operating points. The combination of a reduced blade loading with an incidence correction for lower design point mass flow rates contributes to a slight increase in surge margin for all speed lines. Additionally, the overall efficiency is improved. Toward the choke limit of the 100% and 85% speed lines, the reduced suction side curvature through the lower blade turning is the dominant effect, while the performance under part-load conditions benefits from the incidence correction that is achieved by the adaption of the stagger angle. For the 70% speed line the improvement in isentropic efficiency is less distinct, as the achievable metal angle morphing is too small to alter the largely subsonic blade passage flow. Here the limitation of the effective stagger angle morphing to the upper 30% of the rotor dampens the aerodynamic morphing benefit under the influence of inflow distortion (Figure 7).

Conclusions: Although the perceptible morphing effects are comparably small, both actuator configurations achieve local improvements in fan stage performance. Measured against the main goal to improve the operational efficiency under BLI conditions, the *stagger* + configuration shifts the efficiency islands to lower mass flows, thereby improving the isentropic efficiency at throttled operating conditions. The *turning* + actuation on the contrary provokes higher efficiencies at reduced rotational speeds, but induces an efficiency decrement, when the fan operates at high relative inflow Mach numbers. Here, the induced degradation in peak efficiency amplifies the BLI drawbacks. In relation to the impact, inflow distortion has on an isolated blade passage, the benefits of shape-adaptive fan blading are too small to fully compensate the distortion drawbacks. Therefore, a fan re-design is proposed in order to accelerate the fan's morphing potential.

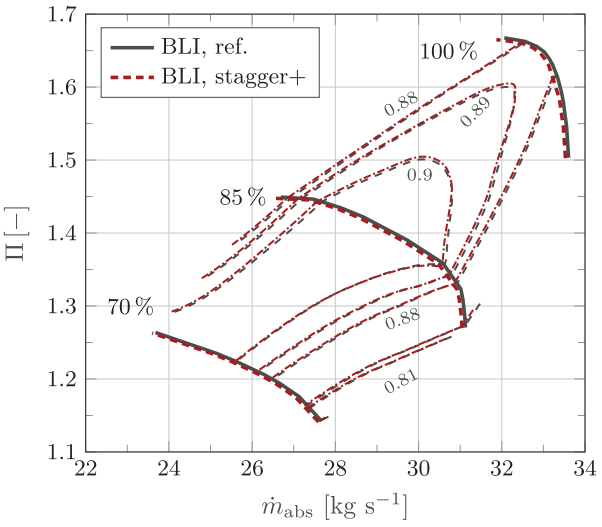

Figure 9. Effect of a blade stagger angle adaption on the rotor performance under BLI influence, displayed for different rotational speeds and the efficiency islands.

3.4. Design of a shape-adaptive fan stage

The chosen NASA rotor 67 test case is therefore substituted by a design, that follows recent UHBR fan design trends. Following Seidler et al. (2024a), a scaled rotor design is chosen, which potentially allows a subsequent test rig application. The potential test rig application defines the maximum fan diameter and yields a hub-to-tip ratio ν_{ht} of 0.26. This corresponds well to recently published fan designs (Eggers et al., 2021) and increases the blade length by 50% compared to the previously investigated NASA rotor 67. The increased blade length requires a load reduction at the blade hub to avoid an extensive overturning. In streamwise direction a slender fan design with an aspect ratio of $AR = 1.95$ is chosen to evoke a lower resistance against the piezoeletric actuation, as described by Seidler et al. (2024a). Compared to literature fan designs, the chosen aspect ratio is higher, which elevates the structural strain on the blade's architecture. The smaller chord lengths additionally increase blade loading and flow diffusion, which is expected to become challenging for part-load

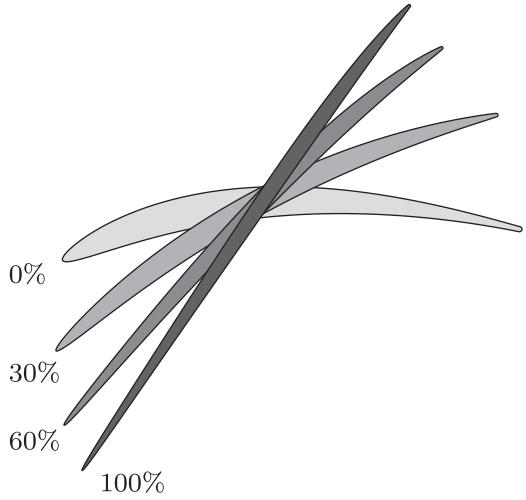

Figure 10. Blade profile sections at different rotor heights.

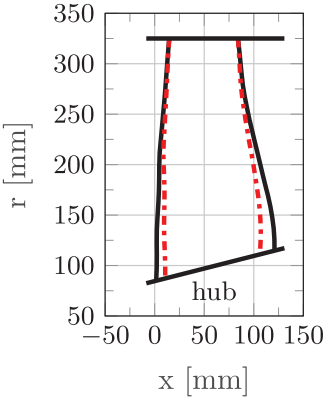

Figure 11. Meridional view of the fan rotor design (black: reference, red: fan design with reduced hub chord length).

efficiency and surge margin. On-design efficiency potentially improves due to lower viscous losses in the shorter blade passage. The off-design drawback is however acceptable as the rotor's shape-adaption capability is tailored to improve efficiency and operational safety during part-load operation. Previous research has shown, that the occurrence of a blade-shock interaction in the tip area of the rotor is beneficial for an amplification of the shape-morphing effect (Seidler et al., 2022). Hence, an axial inflow Mach number of 0.63 is chosen, determining a relative design tip Mach number of 1.2. This results in a design point mass flow of $\dot{m} = 63.33\text{kgs} - 1$ and a rotor pressure ratio of $\Pi = 1.36$. The inflow as well as flow turning for the chosen design point is estimated through a streamline curvature design framework, which predicts an isentropic stage efficiency of $\eta_{is} = 0.92$. For the blade design the extended (Seidler and Friedrichs, 2022) blade modeling approach allows to introduce profiles with increased leading edge thickness for an improved incidence tolerance in the lower 30% of the rotor. For the blade tip, transonic wedge shaped profiles are chosen for a better control over the blade-shock interaction (Figure 10). The span-wise distribution of the blade leading edge, trailing edge and maximum thickness are defined as a ratio of the blade chord to account for structural integrity requirements.

Although the improvement potential for a shape-adaptive fan stage under BLI conditions became apparent, the achievable deformations are too small to significantly alter the drawbacks of ingesting low momentum fluid. With the actuator strength being limited, the blade shape and material remain as design parameters for increasing the shape morphing potential. For the re-design of the blade geometry, especially 3D-design measures are considered as an approach to improve its morphing behavior. Within this investigation, five design parameters are introduced: the hub chord length l_H and the respective sweep and dihedral angles at the blade tip and hub. The effect of a hub chord length reduction is visualized by the red blade edges in Figure 11.

For all design alterations, both actuator configurations from Table 1 are applied, keeping the respective fiber orientation, actuation mechanism and relative actuator dimensions constant. With that constraint, the actuator length is adjusted, depending on the design chord length of the rotor. In span-wise direction, the actuators continue to extend from hub to tip.

3.4.1. Hub chord length. A reduction of the hub chord length leads to a leaner blade shape toward the hub (Figure 11). In radial direction, the hub chord length transitions linearly into to tip chord, which remains constant compared to the blade reference design. To guarantee for the structural integrity of the blade even for reduced chord lengths and profile dimensions, the cross section area of the reference hub section is defined as a boundary condition. Adapting the chord length therefore requires an adjustment of the profile thickness parameters until a similar cross-section area is maintained. Within this investigation, the chord lengths are adjusted between 80% and 110% of its original reference length.

3.4.2. Application of sweep and dihedral. For the evaluation of randomized 3D-adapted blade shapes, a design of experiment (DoE) is conducted with 125 differing parameter combinations. Each design is based on the turbofan reference design and adapted according to the randomly chosen sweep (ϕ_H, ϕ_S) and dihedral (ν_H, ν_S) angles. In case sweep is locally required, the respective chord length is adjusted following equation (5). The parameter space is limited through structural integrity restrictions as well as reasonable aerodynamic sweep and dihedral configurations (see Table 2).

Table 2. Parameter limits for the DoE design space.

Limits	ϕ_H[°]	ϕ_S[°]	ν_H[°]	ν_S[°]
Min	−20	−30	−20	−20
Max	20	20	20	20

For the evaluation of the DoE results, the parameter correlations are considered according to the linear Bravais-Pearson correlation. Following Kronthaler (2014), the correlation analysis yields values between 1 and -1, where negative values indicate an inverse correlation, while correlation parameters below an absolute value of $|p_c| = 0.3$ imply an independence between the respective parameter and the resulting deformations. Additionally, a quadratic approximation is applied to create regression curves and to visualize tendencies in the parameter space.

3.4.3. CFRP blade design. In the structural design process of the CFRP blade architecture, the structural integrity of the blade acts as the primary design constraints. Therefore, a failure analysis is conducted, as the CFRP fan blade will be exposed to operational and morphing loads. One failure criterion employed is the Puck criterion (Puck, 1996), which distinguishes fiber failure, matrix failure, and delamination. Moreover, the maximum stress (*MaxStress*) and strain (*MaxStrain*) criteria of ACP (Ansys Inc, 2022a) are utilized to verify that the respective stress and strain components do not violate their thresholds. Based on an inverse reserve factor of less than 0.66, a laminate with the stacking sequence $(\pm 45_{2f}/ + 22.5_f/0_{2f}/90_{10})/Foam/(90_{10}/0_{2f}/ + 22.5_f/\pm 45_{2f})$ is applied. The 90° unidirectional prepregs with fibers oriented in radial direction primarily carry the centrifugal load, while the woven prepregs cover bending, shearing, and torsional loads, which would otherwise exceed the strength of the epoxy resin matrix. Aerodynamic loads are neglected in the design process, as a detailed load distribution is not available at this stage of the design process.

3.5. Morphing potential of the fan re-design

Both actuator configurations are applied to each reference design variation. The results are summarized in Table 3 and evaluated with respect to the operational requirements of the BLI off-design scenario. For each actuator configuration and rotor design the maximum stagger angle variation $\Delta\lambda$ and the maximum turning angle morphing $\Delta^2\varphi$ at the blade tip are included.

3.5.1. Impact of the fan re-design. Through the increased rotor span, the stagger angle morphing capability is elevated, while the turning morphing capability becomes smaller. For the *stagger +* actuation, the actuation cantilever (length in fiber direction of the actuator) is increased, which elevates the achievable stagger morphing at the blade tip. While the stagger angle morphing capability is increased, morphing the blade turning becomes more difficult. The absolute chord length of the re-designed rotor increases compared to the NASA rotor 67. Although the actuator size becomes bigger, the increased blade chord length determines a higher absolute blade thickness due to structural integrity requirements. The actuators need to deform a stiffer geometry and therefore the blade's resistance against a piezoelectric actuation is elevated. This reduces the deformability and therefore the turning morphing capability of the chosen turbofan design.

Table 3. Morphing results, represented through the maximum morphing values at the blade tip.

Design	*Stagger +*		*Turning +*	
Def.	$\Delta\lambda$ [°]	$\Delta^2\varphi$ [°]	$\Delta\lambda$ [°]	$\Delta^2\varphi$ [°]
NASA 67	0.36	0.02	0.06	0.89
Re-design	0.422	−0.08	0.07	0.79
Hub adp.	0.475	−0.09	0.07	0.86
3D-design	0.51	−0.32	0.15	1.16
CFRP	0.7	0.33	−0.14	1.71

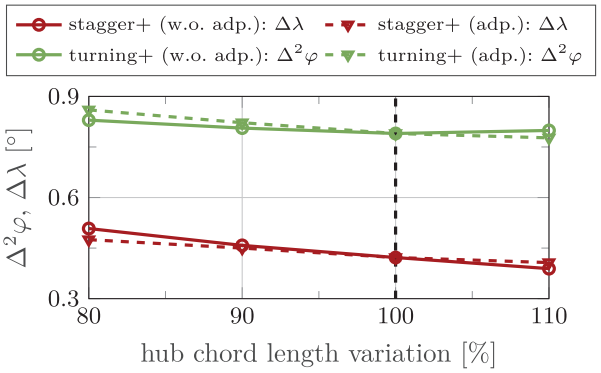

Figure 12. Angular deflections achieved at the blade tip for different hub chord length variations.

3.5.2. Impact of the hub chord length variation. By reducing the hub chord to 80% of its original length, the angular morphing for both actuator configurations is improved (Table 3).

As shown in Figure 12, a *stagger +* actuation benefits from a reduction of the hub chord. This benefit becomes smaller when the thickness of the profile sections is adjusted according to the equal area requirement imposed by the structural integrity boundary condition (*adp.*). For the turning morphing capability (*turning +*) an adverse effect becomes apparent. A rotor design, where the blade thickness parameters are not

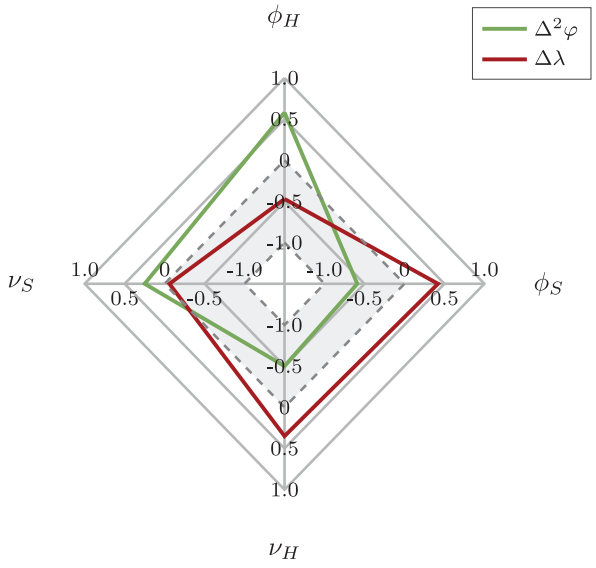

Figure 13. Correlation between 3D-design parameters and achievable angular deformations for the *stagger* + actuation.

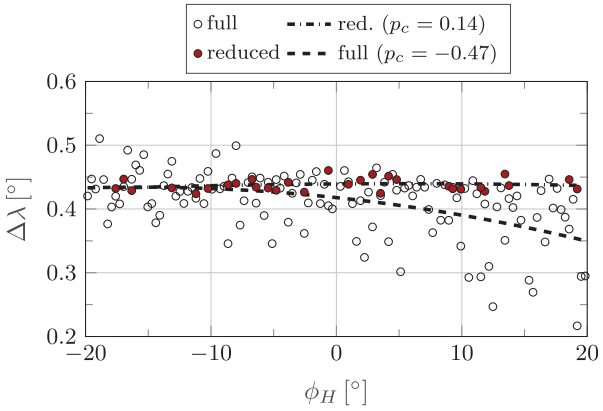

Figure 14. Regression between hub sweep angle ϕ_H and a stagger angle morphing $\Delta\lambda$ for a *stagger* + actuation.

adjusted (*w.o. adp.*) yields a lower increment in morphing potential. Here, the orthogonal distance between actuator surface and blade camber acts as an actuation cantilever. A thicker blade therefore increases the actuation lever, which in turn leads to an elevated turning morphing capability.

3.5.3. Impact of sweep and dihedral. Evaluating the parameter combinations that yield the highest achievable morphing for the respective scenarios ($\Delta\lambda$ for *stagger* + and $\Delta^2\varphi$ for *turning* +) shows that in both cases an increase of the primary morphing target is feasible (Table 3). However, under consideration of the chosen aerodynamic scenario the goal of the actuation is a flow incidence reduction during part-load operation. While the stagger angle morphing is elevated for the *stagger* + actuation, the turning is simultaneously decreased. This dampens the morphing effect on the leading edge metal angle and therefore limits the incidence correction capability. For a targeted evaluation of the 3D-design impact, both relevant angular deformations ($\Delta\lambda$, $\Delta^2\varphi$) need to be considered (Figures 13 and 15).

For the *stagger* + actuation, all but shroud dihedral (ν_S) have an impact on the angular deformations (Figure 13). The strongest nominal correlation is visible for an adaption of the blade turning. Here, the shroud (ϕ_S, $p_c = -0.59$) and the sweep angle (ϕ_H, $p_c = 0.58$) are dominant. Although the actuator configuration is designed to deform the blade twist, sweep and dihedral have the highest impact on the turning morphing potential. The correlations in Figure 13 also indicate that 3D-design measures have an adverse effect on both angular deformations. By choosing positive values for the hub dihedral angle (ν_H) and the shroud sweep angle (ϕ_S) the blade staggering is increased, while the blade turning is reduced. This dependency is also reflected by the design with the highest stagger angle morphing potential in Table 3, where a high stagger morphing potential is diminished by a simultaneous decrease of the blade turning. A similar adverse effect is visible for the hub sweep angle (ϕ_H), where negative angles lead to an increase of the blade staggering and a decrease of the blade turning. Excluding all designs, where the blade turning is decreased or where the stagger angle morphing capability is lower than that of the reference design drastically reduces the number of suitable designs (Figure 14). For the designs left, the correlation between 3D-design measures and stagger angle morphing capability is diminished, as displayed in Figure 14 for the hub sweep angle ϕ_H (reduction indicated by the blue dots). Measured against the chosen operational scenario, the overall impact of blade sweep or dihedral on the stagger angle morphing capability is therefore limited.

With the application of actuators that target the blade turning (*turning* +), 3D-design adaptions have no adverse effect on the angular morphing of blade turning and staggering (Figure 15).

As indicated by the configuration with the highest $\Delta^2\varphi$ value (Table 3) positive shroud sweep angles (ϕ_S) and negative hub dihedral values significantly increase the camber morphing capability of the blade (Figure 8). With a correlation value of $p_c = -0.59$, the hub dihedral angle has the highest impact on the turning morphing capability. Sweep at the hub and dihedral at the shroud on the contrary have a negligible effect. Compared to the fan reference design, where the stagger angle remains unaffected, 3D-design adaptions increasingly induce a morphing of the stagger angle, even though the *turning* + actuation is applied. The highest effect on the stagger angle morphing capability with a correlation parameter of $p_c = 0.86$ is visible for

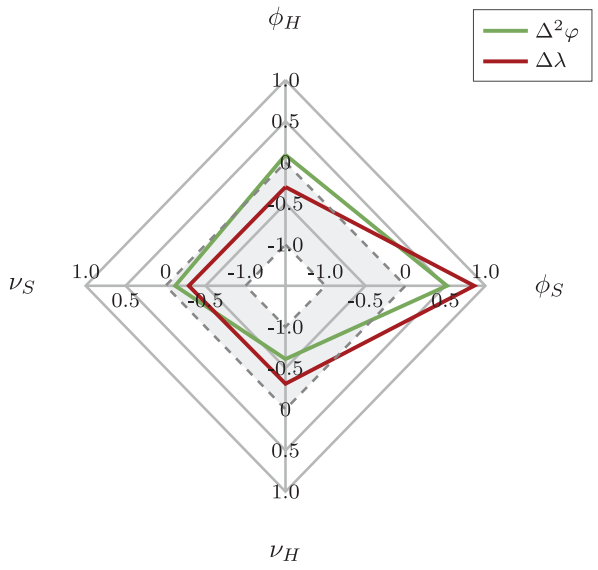

Figure 15. Correlation between 3D-design parameters and achievable angular deformations for a *turning* + actuation.

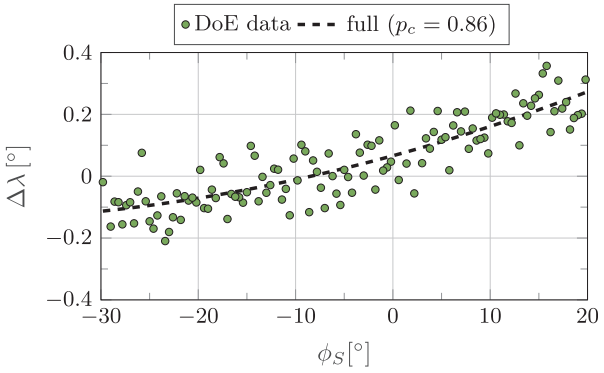

Figure 16. Regression between shroud sweep angle ϕ_S and stagger angle morphing $\Delta\lambda$ for a *turning* + actuation.

the shroud sweep angle ϕ_S, which when increased produces a high stagger angle morphing for the given actuator configuration (Figure 16). Here turning and stagger morphing show a similar geometric dependency - a morphing behavior, which is especially beneficial for the chosen off-design scenario (Figure 15).

3.5.4. Impact of CFRP as blade material. Substituting titanium with CFRP as blade material yields the highest improvement potential within this investigation. According to Table 3, $\Delta^2\varphi$ is increased by 115% to a maximum value of 1.7° for the *turning* + actuation. However, this increase comes with a reduction of the blade staggering by 0.14°, which makes this blade configuration less suitable for the chosen scenario. For the *stagger* + configuration the twist variation values are also significantly increased to a maximum of $\Delta\lambda = 0.7°$ at the blade tip. Simultaneously, the blade turning morphing is amplified with a maximum of $\Delta^2\varphi = 0.33$, which yields a total incidence correction capability of $\Delta i = 0.9°$. The strong increase of the feasible shape morphing is driven by the orthotropy of the chosen fiber laminate. Due to the high centrifugal loads during operation, the unidirectional prepregs are designed to exhibit a high stiffness in span-wise direction of the blade. This induces a lower stiffness orthogonal to the carbon fibers. The *turning* + actuator configuration, with its MFC fiber orientation nearly parallel to the machine axis, exploits the anisotropic stiffness of the blade architecture. This yields an explanation for the significant increase in blade turning morphing capability. The highest benefit for the chosen off-design scenario is however achieved for the *stagger* + actuation, where the anisotropic blade structure leads to a strong coupling between the adaption of blade cambering and twist.

Although the use of CFRP as a material shows significant advantages in terms of morphing performance, thermally induced phenomena must be considered for further maturation, which are not included in the basic analysis presented in the turbofan design section. The manufacturing of a CFRP blade specimen with integrated actuators requires curing temperatures between 80°C and 180°C due to the use of prepregs (Hexcel Corporation, 2025). Although these temperatures are below the Curie temperature of the piezoelectric lead zirconium titanate (PZT) fibers (360°C) applied in the actuators, PZT and the carbon fibers have significantly differing Coefficients of Thermal Expansion (CTE; Płaczek and Kokot, 2019). The piezoelectric PZT fibers of the actuators have a CTE of $3e-6\ °C^{-1}$ (Park and Kim, 2007), while the carbon fibers have a CTE of $-0.47e-6\ °C^{-1}$ (Ansys Inc, 2022b), leading to well understood challenges. Crawley and de Luis (1987) showed that the cooling-related pre-tensioning can result in cracking of the brittle piezoceramic PZT fibers. In addition, tensile strain may lead to depolarization of the piezoelectric material (Mall and Coleman, 1998). In contrast, the use of materials with higher CTEs than PZT (e.g. the titanium alloy with a CTE of $9.4e-6\ °C^{-1}$), allows for a pre-compression of the PZT ceramic, increasing tensile strength and toughness as well as its resistance against depolarization (Barrett et al., 1997; Barrett and Stutts, 1998), ideally suited for the challenging operating conditions found in engines. However, the use of unidirectional CFRP prepregs allows for tailoring of the orthotropic material properties. When the majority of the carbon fibers within the prepreg plies are aligned orthogonally to the PZT fibers within the MFC, the thermal properties of the epoxy resin matrix dominate, which generally has higher CTEs than PZT (Hexcel Corporation, 2025). Future

investigations should therefore investigate how the combination of CTE of the overall CFRP laminate (mixing rule) with the individually orientation of the MFC on the blade affect the pre-stress in the MFCs after cooling. If the challenges prevail, resin infusion processes with cold curing matrix systems can be investigated in more detail. Alternatively, the manufacturing of the blades can include pockets into which the MFCs are inserted after the CFRP laminate has cooled.

4. Summary and conclusion

This research investigated the aerodynamic effects of boundary layer ingestion on an isolated blade passage and how the drawbacks induced can be mitigated by introducing a shape-morphing capability for the fan rotor.

4.1. BLI effects

The BLI induced inflow distortion shifts the speed lines to lower mass flow rates, while the overall peak efficiency of the stage is reduced. To uphold the required thrust of the engine, the fan rotor's work input increases. This elevates blade loading and flow diffusion, especially in the tip region of the rotor. The part-load operating behavior of the fan is accelerated, which reduces the mass flow increment between the current operating point and the stability limit. Usually, the fan is designed for undistorted inflow conditions and the operating point defined by the engine's working line. With flow distortion the inflow velocity is reduced and flow incidence causes the current operating point and the peak efficiency point to diverge. For a full anulus rotor this effect is less distinct, as the distortion pattern investigated is limited to the bottom area of the fan face. The aerodynamic drawbacks for the fan blades passing through the distorted flow regimes are however comparable (Giesecke and Friedrichs, 2019). An approach to align peak efficiency and current operating point is the reduction of the flow incidence in the distorted flow regimes of the rotor. With the goal to reduce flow incidence, two actuator configurations are introduced.

4.2. Shape adaption

The *turning* + scenario achieves this correction by increasing the blade turning and therefore the leading edge camber angle α_1. While an incidence correction is feasible, the increase in blade turning has a more dominant effect. More work is shifted in the tip region of the rotor and flow diffusion is accelerated. The surge margin is further decreased and an efficiency penalty is visible for the transonic 100% speed line. For lower rotational speeds and inflow Mach numbers, the surge margin effect remains, but the peak efficiency of the speed lines is improved. Downstream of the detached leading edge bow shock and for subsonic inflow conditions flow incidence and deviation are improved, which reduces the viscous losses during part-load operation.

The *stagger*+ scenario evokes a speed line shift to lower mass flow rates, thereby increasing the surge margin of the current operating point. With the speed line shift, the mass flow and therefore the achievable total pressure ratio are reduced, which places all speed lines below the BLI reference. Part-load efficiency is slightly increased, which is most distinct for the 100% speed line. Compared to the *turning*+ scenario, the feasible angular morphing is however small and restricted to the upper 30% of the blade height. This limits the overall improvement potential of the *stagger*+ actuator configuration.

4.3. Fan re-design and morphing potential

In relation to the overall BLI effect on the fan performance, both scenarios only show a small improvement potential. A primary target of a shape-adaptive turbofan rotor is therefore the increase of the feasible deformations. Choosing a low hub-to-tip ratio fan design with a slender blade determines an overall higher blade thickness and bigger actuators. While the bigger actuators allow for higher actuation cantilevers, the higher blade thickness elevates the stiffness of the blade, counteracting its morphing capability. For the *turning* + scenario, the thickness effect is dominant and further limits the morphing capability of the fan blade. The *stagger* + scenario on the contrary benefits from the higher actuation cantilevers, which increases the maximum stagger angle morphing at the blade tip by 16%. Three-dimensional design adaptions have shown to further increase the rotor's morphing potential for both actuation concepts. Here, the reduction of the blade hub profile length as a further 3D design measure has a moderate impact. The main effect that is introduced by sweep and dihedral is however not the achievable improvement of the primary morphing parameter, but an alteration of the morphing characteristic. Although the actuator configurations were optimized to affect only the blade turning or the blade twist, three-dimensionally shaping the blade extends the shape morphing to both parameters. For the *stagger*+ actuation, this effect is disadvantageous, as the increase in blade stagger angle morphing capability comes with a reduction of the blade turning. For the chosen operational scenario, both effects are contradictory, when measured against the expected reduction of the inflow incidence i. For actuators that target a stagger angle morphing, the improvement potential of sweep and dihedral is therefore negligible. An actuator fiber orientation that is optimized for a camber angle morphing (*turning*+) on the contrary benefits from a blade 3D-design. The morphing of the blade turning is improved

by 27%, while the maximum increase of the stagger angle by $\Delta\lambda = 0.15°$ fits the requirements of the BLI scenario. Here, a positive shroud sweep angle (ϕ_S) and a negative dihedral at the blade hub (ν_H) have indicated the highest benefit. A forward swept blade at the blade tip is commonly applied to reduce the relative inflow Mach number and therefore reduce shock losses. The dihedral angles on the contrary are unconventional in aerodynamic design. Positive hub dihedral angles are more likely to be used to reduce secondary flow phenomena and therefore losses during part-load operation (Gallimore et al., 2002). As shape-adaptive blading is aiming to avoid part-load operation a compromise in favor of structural deformability is however acceptable.

4.4. Composite material

Most promising for the blade's morphing behavior is the substitution of titanium through a tailored CFRP architecture. By designing the layers of the blade to account for the high rotational loads during operation, the deformability of the blade is increased. Especially, the turning morphing capability could be increased, but with the secondary effect of decreasing the blade staggering. As especially the increase in blade stagger angle has a positive impact on the surge margin, such a deformation is contradictory to the morphing goal within this investigation. Combining a CFRP blade with the *stagger +* actuator configuration shows a higher benefit for the chosen scenario. Here a strong improvement of the stagger angle morphing is combined with a moderate increase in turning angle variation, allowing for an incidence correction of appr. 0.9°. However, in case CFRP is pursued as a blade material, the mismatch of thermal expansion coefficients between carbon fibers and PZT must be considered in order to avoid breakage and depolarization of the piezoelectric fibers during cooling.

5. Outlook

Reducing the complexity of an asymmetric inflow distortion to the investigation of isolated blade passages is a strong simplification of the aerodynamic effects induced by the assumed distortion pattern. Although the chosen simulation approach has proven to be sufficient for the derivation of suitable actuator configurations, full annulus simulations are required to soundly quantify the achievable performance benefits of shape-adaptive fan rotor blading. The preliminary investigation of the interaction of the morphed rotor geometries with the distorted inflow has however shown that the expectable benefit is too small to fully compensate the BLI drawbacks. To accelerate the morphing benefit, different design measures were considered. With the goal of increasing the morphing capability of the fan rotor, an aerodynamically unconventional design was chosen. Especially, the slender rotor design and the chosen dihedral angles deviate from typical fan designs. Their effect on the local fan aerodynamics and the integral fan stage performance needs to be considered in future investigations. Also a combination of the design measures introduced is proposed to further improve the expectable aerodynamic effect. Here, the combination of fiber material structures with 3D-design measures is expected to be promising, as 3D-design adaptions have a significant impact on the deformability and load capacity of the blade. As the design of a shape-adaptive fan rotor blade is a compromise between maintaining structural integrity and providing a sufficient morphing capability, further structural integrity investigations need to conducted, also including the aerodynamic loads the blade experiences throughout a flight mission. The structural investigations proposed should also extend toward experimental investigations to validate the structural morphing methodology. To account for the impact centrifugal and aerodynamic loads have on the morphing behavior of a shape-adaptive fan rotor, stationary structural validation experiments with load equivalents are planned to provide valuable insights for a subsequent application of shape-adaptive turbofan blading in a rotating test rig environment.

Declaration of conflicting interests

The authors declared no potential conflicts of interest with respect to the research, authorship, and/or publication of this article.

Funding

The authors disclosed receipt of the following financial support for the research, authorship, and/or publication of this article: We would like to acknowledge the funding by the Deutsche Forschungsgemeinschaft (DFG, German Research Foundation) under Germany's Excellence Strategy – EXC 2163/1- Sustainable and Energy Efficient Aviation – Project-ID 390881007.

ORCID iD

Felix Kleinwechter https://orcid.org/0009-0003-5150-5367

Data availability statement

The data that support the findings of this study are available from the corresponding author, upon reasonable request.

References

Abate G and Riemenschneider J (2025) Multi-disciplinary and multi-objective optimization problem applied to a morphing blade cascade study. *Journal of Intelligent Material Systems and Structures* 36(2): 119–128.

Ansys Inc (2022a) ACP User's Guide: Release 2022 R2. Canonsburg, PA: Ansys Inc.

Ansys Inc (2022b) Engineering Data User's Guide: Release 2022 R2. Canonsburg, PA: Ansys Inc.

Barbarino S, Saavedra Flores EI, Ajaj RM, et al. (2014) Additive manufacturing of NiTi shape memory alloy and its industrial applications. *Heliyon* 23(6): e23369. DOI: 10.1088/0964-1726/23/6/063001

Barrett R and Stutts J (1998) Development of a piezoceramic flight control surface actuator for highly compressed munitions. In: *39th AIAA/ASME/ASCE/AHS/ASC structures, structural dynamics, and materials conference and exhibit*, p.179. Reston, VA: American Institute of Aeronautics and Astronautics. DOI: 10.2514/6.1998-2034.

Barrett RM, Gross RS and Brozoski FT (1997) Design and testing of a subsonic all-moving adaptive flight control surface. *AIAA Journal* 35(7): 1217–1219.

Benjamin L, Heykena C, Friedrichs J, et al. (2020) Design and optimization of a nacelle for a UHBR turbofan engine using a class shape transformation based parameterization. In: *Proceedings of global power & propulsion society. GPPS*. DOI: 10.33737/gpps20-tc-160.

Bullock RO and Johnson IA (1965) Aerodynamic design of axial-flow compressors. *NASA Special Report* (36).

Crawley EF and de Luis J (1987) Use of piezoelectric actuators as elements of intelligent structures. *AIAA Journal* 25(10): 1373–1385.

Cunnan WS, Stevans W and Urasek DC (1978) Design and performance of a 427-meter-per-second-tip-speed two-stage fan having a 2.40 pressure ratio. Number 1314 in NASA Technical Paper. Cleveland, OH, United States.

Eggers T, Friedrichs J, Goessling J, et al. (2021) Composite UHBR fan for forced response and flutter investigations. In: *Volume 2A: Turbomachinery — Axial 2021*. DOI:10.1115/GT2021-58941.

Eggers T, Kim HR, Bittner S, et al. (2020) Aerodynamic and aeroelastic effects of design-based geometry variations on a low-pressure compressor. *International Journal of Turbomachinery Propulsion and Power* 5(4): 26.

Gallimore SJ, Bolger JJ, Cumpsty NA, et al. (2002) The use of sweep and dihedral in multistage axial flow compressor blading—Part i: University research and methods development. *Journal of Turbomachinery* 124(4): 521–532.

Giesecke D (2022) *Aerodynamic design and performance of an over-wing low pressure ratio fan stage*. Dissertation, Technische Universität Braunschweig and Niedersächsisches Forschungszentrum für Luftfahrt.

Giesecke D, Bullert M, Friedrichs J, et al. (2018) Optimization of high subsonic, high reynolds number axial compressor airfoil sections for increased operating range. *Proceedings of GPPS Forum* 18: 1–9.

Giesecke D and Friedrichs J (2019) Aerodynamic comparison between circumferential and wing-embedded inlet distortion for an ultra-high bypass ratio fan stage. In: *Volume 2A: Turbomachinery 2019*. DOI: 10.1115/GT2019-90425.

Hall CA and Crichton D (2006) Engine and installation configurations for a silent aircraft. *Journal of Turbomachinery* 129(3): 479–487.

Hathaway MD (1986) *Unsteady flows in a single-stage transonic axial-flow fan stator row*. Retrospective theses and dissertations, Iowa State University, Ames.

Hexcel Corporation (2025) Prepreg data sheets: Resources. Available at: https://www.hexcel.com/Resources/Data Sheets/Prepreg (accessed 23 June 2025).

ISO 2533:1975 (1975) *Standard Atmosphere*. Geneva: Standard, International Organization for Standardization.

Karpuk S, Liu Y and Elham A (2020) Multi-fidelity design optimization of a long-range blended wing body aircraft with new airframe technologies. *Aerospace* 7(7): 87.

Kleinwechter F, Seidler M, Monner HP, et al. (2024) Structural design and optimization of piezo-activated morphing CFRP fan blades. In: *ASME 2024 conference on smart materials, adaptive structures and intelligent systems*. American Society of Mechanical Engineers. DOI: 10. 1115/SMASIS2024-139802.

Kovalovs A, Barkanov E and Gluhihs S (2007) Active control of structures using macro-fiber composite (mfc). *Journal of Physics Conference Series* 93: 012034.

Krawczyk P, Beyene A and MacPhee D (2013) Fluid structure interaction of a morphed wind turbine blade. *International Journal of Energy Research* 37(14): 1784–1793.

Krone JH, Huxdorf O, Riemenschneider J, et al. (2017) Experimental investigation and design of a shape-variable compressor cascade. *CEAS Aeronautical Journal* 8(1): 105–127.

Kronthaler F (2014) *Statistik Angewandt*. Berlin, Heidelberg: Springer.

Li C, Pan T, Yan Z, et al. (2023) Aerodynamic characteristics of morphing supersonic cascade under low-upstream-mach-number condition. *AIAA Journal* 61(4): 1708–1719.

Mall S and Coleman JM (1998) Monotonic and fatigue loading behavior of quasi-isotropic graphite/epoxy laminate embedded with piezoelectric sensor. *Smart Materials and Structures* 7(6): 822–832.

Mennicken M, Arzberger MJ and Schnell R (eds.) (2022) Exploring the operational strategy of an electrically-driven variable pitch BLI-Fan. In: *Proceedings of the ISABE conference*. Ottawa, Canada: International Society of Air-Breathing Engines (ISABE).

Park JS and Kim JH (2007) Coefficients of thermal expansion for single crystal piezoelectric fiber composites. *Composites Part B Engineering* 38(7–8): 795–799.

Płaczek M and Kokot G (2019) Modelling and laboratory tests of the temperature influence on the efficiency of the energy harvesting system based on MFC piezoelectric transducers. *Sensors* 19(7): 1558.

Puck A (1996) *Festigkeitsanalyse von Faser-Matrix-Laminaten: Modelle Für Die Praxis*. München and Wien: Hanser.

Schlichting H and Truckenbrodt E (2001) *Aerodynamik Des Flugzeuges: Zweiter Band: Aerodynamik Des Tragflügels (Teil II), Des Rumpfes, der Flügel-Rumpf-Anordnung und der Leitwerke*. Berlin, Heidelberg: Springer.

Schwamborn D, Gerhold T and Heinrich R (2006) The DLR tau-code: Recent applications in research and industry. In: *ECCOMAS CFD 2006 conference*. Available at: https://elib.dlr.de/22421/ (accessed 23 June 2025).

Seidler M, Bode C and Friedrichs J (2024a) Effect of blade reference design variations on the morphing capability of a shape-adaptive fan rotor. *International Journal of Gas Turbine, Propulsion and Power Systems* 15(2): 60–67.

Seidler M and Friedrichs J (2022) Introduction of an improved axial compressor profile shape modelling approach for increased flexibility in transonic profile design. In: *Proceedings of global power & propulsion society. GPPS*. DOI: 10.33737/gpps21-tc-173.

Seidler M, Lück S, Bien M, et al. (2024b) Impact of shape-adaptive fan blading on the performance of a turbofan engine. In: *GPPS Chania 2024 proceedings*, pp.1–14. DOI: 10.33737/gpps24-tc-184.

Seidler M, Montano Z, Friedrichs J, et al. (eds) (2022) Introduction and evaluation of an aerostructural coupling approach for the design of shape adaptive compressor blading. In: *Proceedings of ISABE 2022*.

Smart Material GmbH (2023) MFC engineering properties. Available at: https://smart-material.com/wp-content/uploads/2025/02/MFC_V2.4-datasheet-web.pdf (accessed 23 June 2025).

Smith LH (2023) Wake ingestion propulsion benefit. *Journal of Propulsion and Power* 9(1): 74–82.

Suman A, Fortini A, Aldi N, et al. (2017) Analysis of the aerodynamic and structural performance of a cooling fan with morphing blade. *International Journal of Turbomachinery Propulsion and Power* 2(2): 7.

Tweedt DL (2013) *Preliminary aerodynamic investigation of fan rotor blade morphing*. Number CR-2012-217815 in Technical Report. Cleveland, OH, United States.

Voigt J and Friedrichs J (2021) Development of a multi-segment parallel compressor model for a boundary layer ingesting fuselage fan stage. *Energies* 14(18): 5746.

Appendix

Notation

κ	Blade metal angle
λ	Blade stagger angle
φ	Blade turning angle
$(.)_0$	Far field
$(.)_1$	Leading edge
$(.)_H$	Hub
$(.)_S$	Shroud
α	Leading edge camber angle
β	Relative inflow angle
$\dot{m}$	Mass flow
η	Efficiency
ν	Dihedral angle
$\nu_h t$	Hub to tip ratio
ϕ	Sweep angle
π	Pressure ratio
AR	Aspect ratio
i	Incidence angle
l	Chord length
r	Radius
V_m	Meridional velocity
p_c	Correlation parameter
p_t	Total pressure
y^+	Dimensionless wall distance
abs	Absolute
BLI	Boundary layer ingestion
BWB	Blended wing body
CAD	Computer aided design
CFD	Computational fluid dynamics
CFRP	Carbon fiber reinforced polymers
def	Deformed
DoE	Design of experiment
FEA	Finite element analysis
is	Isentropic
ISA	International Standard Atmosphere
MFC	Macro-fiber-composite
PS	Pressure side
ref	Reference
SLC	Streamline curvature
SS	Suction side
UHBR	Ultra high bypass ratio